



Article

Event Rates for the Scattering of Weakly Interacting Massive Particles from ^{23}Na and ^{40}Ar

R. Sahu ^{1,*}, V. K. B. Kota ² and T. S. Kosmas ³¹ National Institute of Science and Technology, Palur Hills, Berhampur 761008, India² Physical Research Laboratory, Ahmedabad 380 009, India; vkbkota@prl.res.in³ Division of Theoretical Physics, University of Ioannina, GR 45110 Ioannina, Greece; hkosmas@uoi.gr

* Correspondence: rankasahu@gmail.com; Tel.: +91-700-820-8393

Abstract: Detection rates for the elastic and inelastic scattering of weakly interacting massive particles (WIMPs) off ^{23}Na are calculated within the framework of Deformed Shell Model (DSM) based on Hartree-Fock states. At first, the spectroscopic properties of the detector nucleus, like energy spectra and magnetic moments, are evaluated and compared with experimental data. Following the good agreement of these results, DSM wave functions are used for obtaining elastic and inelastic spin structure functions, nuclear structure coefficients and so forth for the WIMP- ^{23}Na scattering. Then, the event rates are also computed with a given set of supersymmetric parameters. In the same manner, using DSM wavefunctions, nuclear structure coefficients and event rates for elastic scattering of WIMPs from ^{40}Ar are also obtained. These results for event rates and also for annual modulation will be useful for the ongoing and future WIMP detection experiments involving detector materials with ^{23}Na and ^{40}Ar nuclei.

Keywords: deformed shell model; ^{23}Na and ^{40}Ar ; dark matter detection



Citation: Sahu, R.; Kota, V.K.B.; Kosmas, T.S. Event Rates for the Scattering of Weakly Interacting Massive Particles from ^{23}Na and ^{40}Ar . *Particles* **2021**, *4*, 75–92. <https://doi.org/10.3390/particles4010010>

Received: 11 January 2021
Accepted: 17 February 2021
Published: 24 February 2021

Publisher's Note: MDPI stays neutral with regard to jurisdictional claims in published maps and institutional affiliations.



Copyright: © 2021 by the authors. Licensee MDPI, Basel, Switzerland. This article is an open access article distributed under the terms and conditions of the Creative Commons Attribution (CC BY) license (<https://creativecommons.org/licenses/by/4.0/>).

1. Introduction

During the last three decades, the satellite missions of the Cosmic Background Explorer (COBE) [1], the Wilkinson Microwave Anisotropy Probe (WMAP) [2] and the Planck space telescope [3,4] launched into space with the aim of exploring Cosmic Microwave Background (CMB) radiation [5]. Nowadays, from the data of these missions and also those of the Supernova Cosmology Project (SCP) [6], it is well known that this ancient light reveals secrets of the origin of the Universe. Moreover, from the data of the most advanced satellite PLANCK (a mission of ESA with significant participation from NASA), researchers (cosmologists, astronomers and physicists) have concluded that most of the universe's mass is cold, dark and non-baryonic [2]. In addition, the more recent CMB measurements by PLANCK support that CMB is strongly anisotropic.

Despite the intensive experimental effort and employment of extremely sensitive and very low-energy threshold nuclear detectors, up to now, non-baryonic cold dark matter candidates have not been observed and, hence, its nature is still a mystery. It is, however, worth mentioning that the Axion Dark Matter Experiment (ADMX), at Washington University, very recently announced as “the first experiment that achieved the sensitivity to hunt for dark matter (DM) axions (axions are known as CDM candidates, not yet observed) [7].

Furthermore, the most promising non-baryonic cold dark matter candidates are the Weakly Interacting Massive Particles (WIMPs), which arise in super symmetric theories of physics beyond the standard model. The most appealing WIMP candidate is the Lightest Supersymmetric Particle (LSP) (lightest neutralino), which is expected to be stable and to interact very weakly with matter [5,8,9].

There are many experimental efforts [10–13] to detect WIMPs via their scattering from the nuclei of the detector providing finger-prints regarding their existence. Some of these are the Super CDMS SNOLAB project, XENON1T, PICO-60, EDELWEISS and so on; see, for

example, [13–16]. Nuclear isotopes like ^{23}Na , ^{40}Ar , ^{71}Ga , ^{73}Ge , ^{75}As , ^{127}I , ^{133}Cs and ^{133}Xe , are among the popular detector nuclei; see [12,13,17] and references therein. Our focus in this paper is on ^{23}Na (the only stable isotope in the natural Na) and ^{40}Ar (with 99.59% abundance in the natural Ar). The DAMA/NaI and DAMA/LiBRA [18] experiments investigated the presence of dark matter particles in the galactic halo using the NaI(Tl) detector (the only Na isotope in NaI is the ^{23}Na).

In these experiments, the predicted annual modulation was not yet confirmed [13], though a signal of annual modulation in NaI was reported in [19]. However, the SABRE experiment [20] aims to directly measure the annual modulation of the dark matter interaction rate with NaI(Tl) crystals. Other related experiments with NaI detectors are ANAIS [21] and DM-Ice [22]. Also, there are the important DARKSIDE-50 [23] and DEAP-3600 [24] and DarkSide-20k [25] experiments using liquid Argon (with ^{40}Ar) as a detector.

It should be noted that direct detection experiments are exposed to various neutrino emissions [26–29]. The interaction of these neutrinos, especially the astrophysical ones, with the material of the dark matter detectors, known as the neutrino-floor, is a serious background source. Recently the coherent elastic scattering of neutrinos off nuclei ($\text{CE}\nu\text{NS}$) has been observed at the Spallation Neutron Source at the Oak Ridge National Laboratory [30] employing the facilities used in the direct detection of dark matter searches. The impact of the neutrino floor on the relevant experiments looking for cold dark matter was extensively investigated for example in [26].

There are many theoretical calculations that describe different aspects of the direct detection of dark matter through the recoil-energy of the nucleus in WIMP-nucleus scattering. For elastic scattering, we need to consider the spin-spin interaction coming from the axial current and also the dominant scalar interaction. For the inelastic part, scalar interaction practically does not contribute. The scalar interaction can arise from the squark exchange, the Higgs exchange, the interaction of WIMPs with gluons and so forth. A more general non-relativistic effective field theory approach for WIMP-nucleus scattering was developed by Haxton and collaborators [31,32]. There is also the chiral effective field theory approach; see [33]. Suhonen and his collaborators have performed a series of truncated shell model calculations for WIMP-nucleus scattering [34–38].

In these studies, for example, they have calculated the event rates for WIMP-nucleus elastic and inelastic scattering for ^{83}Kr and ^{125}Te [38] and also ^{127}I , $^{129,131}\text{Xe}$ and ^{133}Cs [36]. In addition, recently Vergados et al. [39] examined the possibility of detecting electrons in the searches for light WIMP with a mass in the MeV region and found that the events of 0.5–2.5 per kg-y would be possible; this idea was also proposed earlier by the authors of [40]. A few years back, full large-scale shell-model calculations were carried out in [17,41] for WIMP scattering of $^{129,131}\text{Xe}$, ^{127}I , ^{73}Ge , ^{19}F , ^{23}Na , ^{27}Al and ^{29}Si nuclei. Baudis et al. [42] have explored the inelastic scattering of the dark matter of nuclei within the shell model and chiral effective field theory. Finally, using the large scale shell model [33] and coupled cluster theory [43], WIMP-nucleus and neutrino-nucleus scattering, respectively, with ^{40}Ar target have been studied.

In recent years, the deformed shell model (DSM), based on Hartree-Fock (HF), deformed intrinsic states with angular momentum projection and band mixing, has been established to be a good model to describe the properties of nuclei in the mass range $A = 60\text{--}90$ [44]. Among many applications, DSM is found to be quite successful in describing the spectroscopic properties of medium heavy $N = Z$ odd-odd nuclei with isospin projection [45], double beta decay half-lives [46,47] and $\mu - e$ conversion in the field of the nucleus [48]. Going beyond these applications, recently we have studied the event rates for WIMP with ^{73}Ge as the detector [49]. In addition to the energy spectra and magnetic moments, the model is used to calculate the spin structure functions and the nuclear form factors (nuclear matrix elements) for the elastic and inelastic CDM scattering.

Following the aforementioned successful studies, we have recently used DSM for the evaluation of the neutrino-floor due to coherent elastic neutrino-nucleus scattering ($\text{CE}\nu\text{NS}$) [26] for the detector nuclei ^{73}Ge , ^{71}Ga , ^{75}As and ^{127}I . We considered well known

neutrino sources as solar- ν , atmospheric- ν as well as the diffused supernova neutrino background (DSNB) and found that the neutrino-floor contributions may lead to a distortion of the expected recoil spectrum, limiting the sensitivity of the direct dark matter search experiments. In [12], DSM results for WIMP scattering from ^{127}I , ^{133}Cs and ^{133}Xe are described in detail. To complete these studies, using DSM for the nuclear structure part, in the present paper we will present results for WIMP- ^{23}Na elastic and inelastic scattering and WIMP- ^{40}Ar elastic scattering.

The rest of the paper is organized as follows—Section 2 gives, for completeness and easy reading of the paper, a brief discussion of the formulation of WIMP-nucleus elastic and inelastic scattering and event rates. In Section 3 the DSM formulation is described with examples drawn from ^{75}As spectroscopic results. In Section 4 spectroscopic results and also the results for the elastic and inelastic scattering of WIMPs from ^{23}Na are presented. Similarly, WIMP- ^{40}Ar elastic scattering results are presented in Section 5. The results in Sections 4 and 5 are the main results of this paper. Finally, concluding remarks are made in Section 6.

2. Event Rates for WIMP-Nucleus Scattering

WIMP flux on earth coming from the galactic halo is expected to be quite large, of the order 10^5 per cm^2 per second. Even though the interaction of WIMPs with matter is weak, this flux is sufficiently large for the galactic WIMPs to deposit a measurable amount of energy in an appropriately sensitive detector apparatus when they scatter off nuclei. Most of the experimental searches of WIMP are based on direct detection through their interaction with nuclei in the detector. The relevant theory of WIMP-nucleus scattering is well known as available in the papers by Suhonen and his group and also in our earlier papers mentioned above [34–36,38,49]. For completeness we give here a few important steps. In the case of spin-spin interaction, the WIMP couples to the spin of the nucleus and, in the case of scalar interaction, the WIMP couples to the mass of the nucleus. In the expressions for the event rates, the particle physics part is separated from the nuclear part so that the role played by the nuclear part becomes apparent.

2.1. Elastic Scattering

The differential event rate per unit detector mass for a WIMP with mass m_χ can be written as [5],

$$dR = N_t \phi f \frac{d\sigma}{d|q|^2} d^3v d|q|^2. \tag{1}$$

Here, ϕ , which is equal to $\rho_0 v / m_\chi$, is the dark matter flux with ρ_0 being the local WIMP density. Similarly, N_t stands for the number of target nuclei per unit mass and f is the WIMP's velocity distribution which is assumed to be of Maxwell-Boltzmann type [which is modified in other halo models (see for example [50]) but we did not consider these in the present paper]. It takes into account the distribution of the WIMP velocity relative to the detector (or earth) and also the motion of the sun and earth. If we neglect the rotation of the earth about its own axis, then $v = |\mathbf{v}|$ is the relative velocity of WIMP with respect to the detector. Also, q represents the momentum transfer to the nuclear target, which is related to the dimensionless variable

$$u = \frac{1}{2} q^2 b^2,$$

with b being the oscillator length parameter. The WIMP-nucleus differential cross section in the laboratory frame is given by [34–36,38,49]

$$\frac{d\sigma(u, v)}{du} = \frac{1}{2} \sigma_0 \left(\frac{1}{m_p b} \right)^2 \frac{c^2}{v^2} \frac{d\sigma_A(u)}{du}. ; \tag{2}$$

with

$$\begin{aligned} \frac{d\sigma_A(u)}{du} = & (f_A^0)^2 F_{00}(u) + 2f_A^0 f_A^1 F_{01}(u) + (f_A^1)^2 F_{11}(u) \\ & + \left[Z(f_S^0 + f_S^1) \right]^2 |F_Z(u)|^2 \\ & + \left[(A - Z)(f_S^0 - f_S^1) \right]^2 |F_N(u)|^2 \\ & + 2Z(A - Z) \left[(f_S^0)^2 - (f_S^1)^2 \right] |F_Z(u)||F_N(u)|, \end{aligned} \tag{3}$$

where $F_Z(u)$ and $F_N(u)$ denote the nuclear form factors for protons and neutrons, respectively. In Equation (2), the parameter $\sigma_0 = 0.77 \times 10^{-38} \text{ cm}^2$ and the mass of proton $m_p = 1.67 \times 10^{-27} \text{ kg}$. In Equation (3), the first three terms correspond to spin contribution coming mainly from the axial current and the other three terms stand for the coherent part coming mainly from the scalar interaction. Here, f_A^0 and f_A^1 represent the isoscalar and isovector parts of the axial vector current and similarly f_S^0 and f_S^1 represent isoscalar and isovector parts of the scalar current. The nucleonic current parameters f_A^0 and f_A^1 depend on the specific SUSY model employed. However, f_S^0 and f_S^1 depend, beyond the SUSY model, on the hadron model used to embed quarks and gluons into nucleons. The normalized spin structure functions $F_{\rho\rho'}(u)$ with $\rho, \rho' = 0,1$ are defined as

$$\begin{aligned} F_{\rho\rho'}(u) = & \sum_{\lambda,\kappa} \frac{\Omega_\rho^{(\lambda,\kappa)}(u)\Omega_{\rho'}^{(\lambda,\kappa)}(u)}{\Omega_\rho\Omega_{\rho'}}; \\ \Omega_\rho^{(\lambda,\kappa)}(u) = & \sqrt{\frac{4\pi}{2J_i+1}} \\ & \times \langle J_f || \sum_{j=1}^A [Y_\lambda(\Omega_j) \otimes \sigma(j)]_{\kappa} j_\lambda(\sqrt{u}r_j)\omega_\rho(j) || J_i \rangle. \end{aligned} \tag{4}$$

In the above equation $\omega_0(j) = 1$ and $\omega_1(j) = \tau(j)$; note that $\tau = +1$ for protons and -1 for neutrons and j_λ is the spherical Bessel function. The static spin matrix elements are defined as $\Omega_\rho(0) = \Omega_\rho^{(0,1)}(0)$. Now, the event rate can be written as

$$\langle R \rangle = \int_{-1}^1 d\tilde{\xi} \int_{\psi_{min}}^{\psi_{max}} d\psi \int_{u_{min}}^{u_{max}} G(\psi, \tilde{\xi}) \frac{d\sigma_A(u)}{du} du. \tag{5}$$

In the above, $G(\psi, \tilde{\xi})$ is given by

$$G(\psi, \tilde{\xi}) = \frac{\rho_0}{m_\chi} \frac{\sigma_0}{Am_p} \left(\frac{1}{m_p b} \right)^2 \frac{c^2}{\sqrt{\pi}v_0} \psi e^{-\lambda^2} e^{-\psi^2} e^{-2\lambda\psi\tilde{\xi}}. \tag{6}$$

Here, $\psi = v/v_0$, $\lambda = v_E/v_0$, $\tilde{\xi} = \cos(\theta)$. Parameters used in the calculation are as follows. Firstly, the WIMP density $\rho_0 = 0.3 \text{ GeV/cm}^3$. The velocity of the sun with respect to the galactic centre is taken to be $v_0 = 220 \text{ km/s}$ and the velocity of the earth relative to the sun is taken as $v_1 = 30 \text{ km/s}$. The velocity of the earth with respect to the galactic centre v_E is given by $v_E = \sqrt{v_0^2 + v_1^2 + 2v_0v_1 \sin(\gamma)\cos(\alpha)}$, where α is the modulation angle which stands for the phase of the earth on its orbit around the sun and γ is the angle between the normal to the elliptic and the galactic equator, which is taken to be $\simeq 29.8^\circ$. Using the notations, $X(1) = F_{00}(u)$, $X(2) = F_{01}(u)$, $X(3) = F_{11}(u)$, $X(4) = |F_Z(u)|^2$, $X(5) = |F_N(u)|^2$, $X(6) = |F_Z(u)||F_N(u)|$ the event rate per unit mass of the detector is given by

$$\begin{aligned}
 \langle R \rangle_{el} = & (f_1^0)^2 D_1 + 2f_A^0 f_A^1 D_2 + (f_A^1)^2 D_3 \\
 & + \left[Z(f_S^0 + f_S^1) \right]^2 D_4 \\
 & + \left[(A - Z)(f_S^0 - f_S^1) \right]^2 D_5 \\
 & + 2Z(A - Z) \left[(f_S^0)^2 - (f_S^1)^2 \right] D_6,
 \end{aligned} \tag{7}$$

where D_i is the three dimensional integrations of Equation (5), defined as

$$D_i = \int_{-1}^1 d\xi \int_{\psi_{min}}^{\psi_{max}} d\psi \int_{u_{min}}^{u_{max}} G(\psi, \xi) X(i) du. \tag{8}$$

The lower and upper limits of integrations given in Equations (5) and (8) have been worked out by Pirinen et al. [38] and they are

$$\psi_{min} = \frac{c}{v_0} \left(\frac{Am_p Q_{thr}}{2\mu_r^2} \right)^{1/2} \tag{9}$$

$$\psi_{max} = -\lambda\xi + \sqrt{\lambda^2 \xi^2 + \frac{v_{esc}^2}{v_0^2} - 1 - \frac{v_1^2}{v_0^2} - \frac{2v_1}{v_0} \sin(\gamma) \cos(\alpha)}. \tag{10}$$

With the escape velocity v_{esc} from our galaxy being 625 km/s, the value of $v_{esc}^2/v_0^2 - 1 - v_1^2/v_0^2$ appearing in Equation (10) is 7.0525. Similarly, the value of $(2v_1/v_0)\sin(\gamma)$ is 0.135. The values of u_{min} and u_{max} are $Am_p Q_{thr} b^2$ and $2(\psi\mu_r b v_0/c)^2$, respectively. Here, Q_{thr} is the detector threshold energy and μ_r is the reduced mass of the WIMP-nucleus system.

2.2. Inelastic Scattering

In the inelastic scattering the entrance channel and exit channel are different. The inelastic scattering cross section due to scalar current is considerably smaller than the elastic case and hence it is neglected. Hence, we focus on spin dependent scattering. The inelastic event rate per unit mass of the detector can be written as

$$\langle R \rangle_{in} = (f_1^0)^2 E_1 + 2f_A^0 f_A^1 E_2 + (f_A^1)^2 E_3, \tag{11}$$

where E_1, E_2 and E_3 are the three dimensional integrations

$$E_i = \int_{-1}^1 d\xi \int_{\psi_{min}}^{\psi_{max}} d\psi \int_{u_{min}}^{u_{max}} G(\psi, \xi) X(i) du. \tag{12}$$

The limits of integration for E_1, E_2 and E_3 are [36,38]

$$u_{min(max)} = \frac{1}{2} b^2 \mu_r^2 \frac{v_0^2}{c^2} \psi^2 \left[1 \mp \sqrt{1 - \frac{\Gamma}{\psi^2}} \right]^2, \tag{13}$$

where

$$\Gamma = \frac{2E^* c^2}{\mu_r c^2 v_0^2}, \tag{14}$$

with E^* being the energy of the excited state. ψ_{max} is the same as in the elastic case and the lower limit $\psi_{min} = \sqrt{\Gamma}$. Baudis et al. [42] have used the same expression for the lower limit ψ_{min} . The parameters ρ_0, σ_0 and so forth have the same values as in the elastic case.

3. Deformed Shell Model

The nucleonic current part has been separated from the nuclear part in the expression for the event rates for elastic and inelastic scattering given by Equations (7) and (11) respectively with $X(i)$ giving the nuclear structure part. However, the D_i 's and E_i 's depend not only on the nuclear structure part but also on the kinematics and assumptions on the WIMP velocity. The evaluation of $X(i)$ depends on spin structure functions and the form factors. We have used DSM for the evaluation of these quantities. Here, for a given nucleus, starting with a model space consisting of a given set of single particle (sp) orbitals and effective two-body Hamiltonian (TBME + spe), the lowest energy intrinsic states are obtained by solving the Hartree-Fock (HF) single particle equation self-consistently. We assume axial symmetry. For example, Figure 1 shows the HF single particle spectrum for ^{75}As corresponding to the lowest prolate intrinsic state. Used here are the spherical sp orbits $1p_{3/2}$, $0f_{5/2}$, $1p_{1/2}$, and $0g_{9/2}$ with energies 0.0, 0.78, 1.08, and 3.20 MeV, respectively, while the assumed effective interaction is the modified Kuo interaction [51]. Excited intrinsic configurations are obtained by making particle-hole excitations over the lowest intrinsic state. These intrinsic states $\chi_K(\eta)$ do not have definite angular momenta. Hence, states of good angular momentum are projected from an intrinsic state $\chi_K(\eta)$ and they can be written as,

$$\psi_{MK}^J(\eta) = \frac{2J+1}{8\pi^2\sqrt{N_{JK}}} \int d\Omega D_{MK}^{J*}(\Omega) R(\Omega) |\chi_K(\eta)\rangle \quad (15)$$

where N_{JK} is the normalization constant. In Equation (15), Ω represents the Euler angles (α, β, γ) and $R(\Omega)$, which is equal to $\exp(-i\alpha J_z)\exp(-i\beta J_y)\exp(-i\gamma J_z)$, which represents the general rotation operator. The good angular momentum states projected from different intrinsic states are not in general orthogonal to each other. Hence they are orthonormalized and then band mixing calculations are performed. This gives the energy spectrum and the eigenfunctions. Figure 2 shows the calculated energy spectrum for ^{75}As as an example. In the DSM band mixing calculations used are six intrinsic states [26]. Let us add that the eigenfunctions are of the form

$$|\Phi_M^J(\eta)\rangle = \sum_{K,\alpha} S_{K\eta}^J(\alpha) |\psi_{MK}^J(\alpha)\rangle. \quad (16)$$

The nuclear matrix elements entering the calculation of magnetic moments, elastic and inelastic spin structure functions and so forth are evaluated using the wave function $\Phi_M^J(\eta)$. For example, the calculated magnetic moments for the $3/2_1$, $3/2_2$ and $5/2_1$ states are (in nm units) 1.422, 1.613 and 0.312 compared to experimental values [52] 1.439, 0.98 and 0.98 respectively. The calculated values are obtained using bare gyromagnetic ratios and the results will be better for the excited states if we take $g_\ell^p = 0.5$, $g_\ell^n = 0.7$, $g_s^p = 4$ and $g_s^n = -3$. The neutron spin part is small and hence does not appreciably contribute to the magnetic moments of the above three states. The use of effective g -factors is advocated in [53].

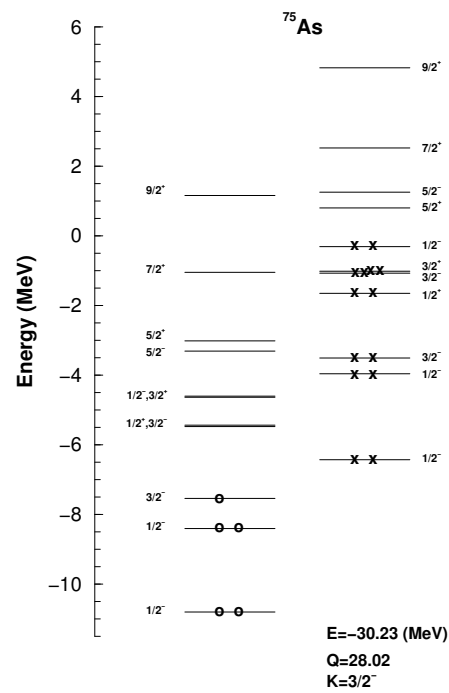


Figure 1. Hartree-Fock (HF) single-particle spectra for ^{75}As corresponding to lowest prolate configuration. In the figure, circles represent protons and crosses represent neutrons. The HF energy E in MeV, mass quadrupole moment Q in units of the square of the oscillator length parameter and the total azimuthal quantum number K are given in the figure.

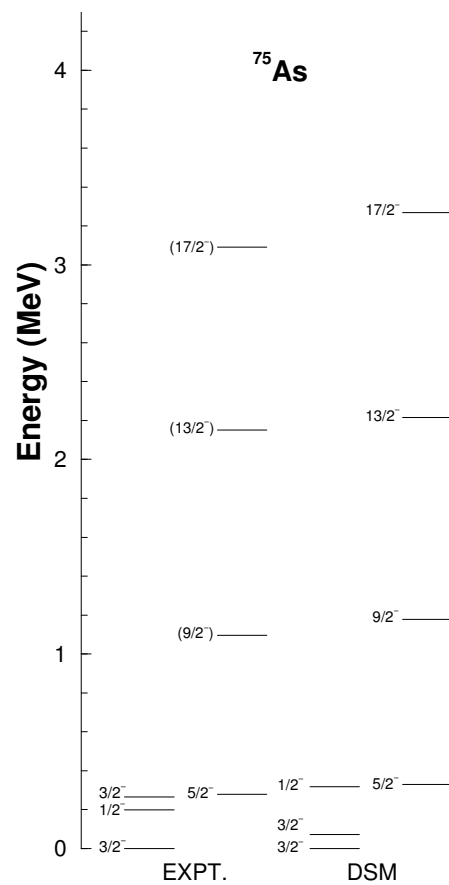


Figure 2. Comparison of Deformed Shell Model (DSM) results with experimental data for ^{75}As for collective bands with negative parity. The experimental values are taken from [52].

4. Results for WIMP-²³Na Scattering

The nuclear structure plays an important role in studying the event rates in WIMP-nucleus scattering. Hence, we first calculate the energy spectra and magnetic moments within our DSM model for ²³Na. Agreement with experimental data will provide information regarding the goodness of the wave functions used. This in turn will give us confidence regarding the reliability of our predictions of event rates. These spectroscopic results are presented in Section 4.1. Let us add that in Sections 4.2 and 4.3 the value of the oscillator length parameter b is needed and it is taken to be 1.573 fm for ²³Na. In our earlier work in the calculation of transition matrix elements for $\mu - e$ conversion in ⁷²Ge [48], we had taken the value of this length parameter as 1.90 fm. Assuming $A^{1/6}$ dependence, the above value of the oscillator parameter is chosen for ²³Na. Let us add that, in the quasi-particle random phase approximation (QRPA), the harmonic oscillator size parameter is calculated through the following semi-empirical formulas. For light nuclear isotopes the formula used is $b_l = 6.4396(a/41)^{1/2}$, where $a = A^{1/3}$ with A being the mass number of the studied nucleus. For heavy nuclear isotopes it is $b_h = 6.4396[(a + 1.41)/53]^{1/2}$. Then, the mean value is $b_{mean} = (b_l + b_h)/2$ and in many works using QRPA this mean value is employed [17].

4.1. Spectroscopic Results

In the ²³Na calculations, ¹⁶O is taken as the inert core with the spherical single particle orbitals $0d_{5/2}$, $1s_{1/2}$ and $0d_{3/2}$ generating the basis space. “USD” interaction of Wildenthal with sp energies -3.9478 , -3.1635 and 1.6466 MeV has been used in the calculation [54]. This effective interaction is known to be quite successful in describing most of the important spectroscopic features of nuclei in the $1s0d$ -shell region [54]. For this nucleus, the calculated lowest HF single particle spectrum of prolate shape is shown in Figure 3. The odd proton is in the $k = 3/2^+$ deformed single particle orbit. The excited configurations are obtained by particle-hole excitations over this lowest configuration. We have considered a total of five intrinsic configurations. As described above, angular momentum states are projected from each of these intrinsic configurations and then a band mixing calculation is performed. The band mixed wave functions $S_{K\eta}^J$ defined in Equation (16) are used to calculate the energy levels, magnetic moments and other properties of this nucleus.

The calculated levels are classified into collective bands on the basis of the E2 transition probabilities between them. The results for the lowest positive parity band for ²³Na are shown in Figure 4. The experimental data are from Reference [52]. For this nucleus, the ground state is $3/2^+$, which is reproduced in our calculation. A positive parity band built on $3/2^+$ has been identified for this nucleus. This band is quite well reproduced by the DSM calculation. An analysis of the wave functions shows that this band mainly originates from the lowest HF intrinsic configuration shown in Figure 3. However, there are admixtures from the good angular momentum states coming from other intrinsic configurations. The wavefunction coming from the lowest HF intrinsic configuration slightly increases in value with increased angular momentum. This shows that the collectivity of this band does not change appreciably at higher angular momentum. Since we are considering WIMP-nucleus scattering from a ground state and low lying positive parity states, the negative parity bands are not important for the present purpose.

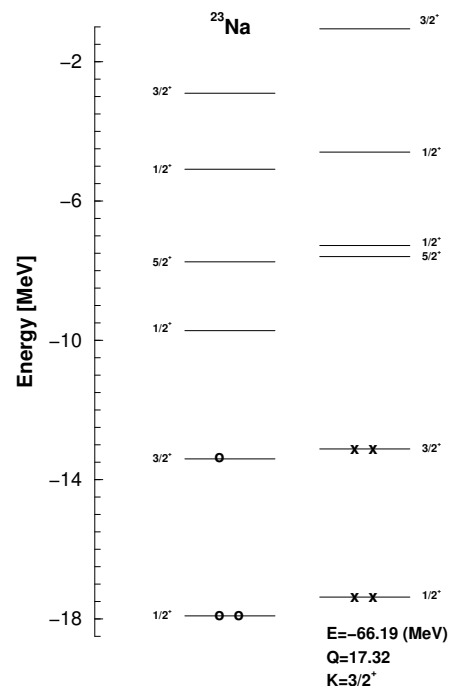


Figure 3. HF single-particle spectra for ^{23}Na corresponding to lowest configuration. In the figure, circles represent protons and crosses represent neutrons. The HF energy E in MeV, mass quadrupole moment Q in units of the square of the oscillator length parameter and the total azimuthal quantum number K are given in the figure.

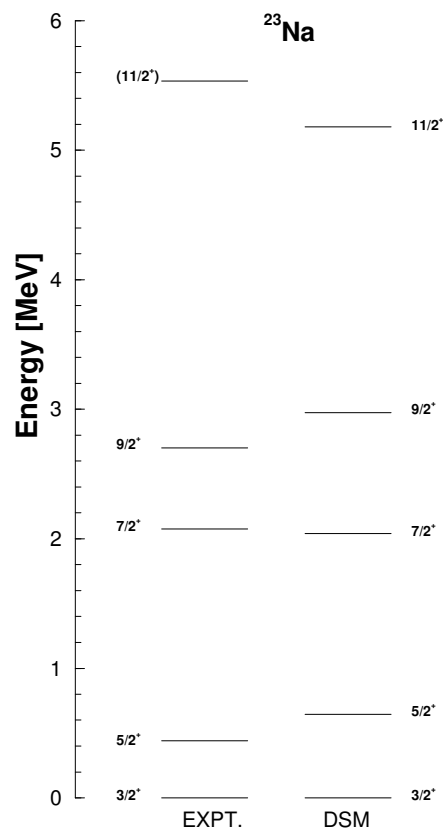


Figure 4. Comparison of deformed shell model results with experimental data for ^{23}Na for yrast band which is of positive parity. The experimental values are taken from [52].

In the calculation of the event rates, spin plays an important role. Hence, the magnetic moment of various low-lying levels in ^{23}Na are calculated. The result for the ground state of the lowest $K = 3/2^+$ band is 2.393 nm and the corresponding available experimental data value is 2.218 nm. The contribution of protons and neutrons to the orbital parts are 0.957 and 0.262 and to the spin parts are 0.267 and 0.014, respectively. This decomposition gives better physical insight. The calculated value of magnetic moment for the ground state agrees quite well with experimental data [52]. Let us add that there are no experimental data for the magnetic moments of the excited states. An approach with state-dependent gyromagnetic moments, as advocated for example in [53], better reproduces the experimental magnetic moments. The DSM spectroscopic results are also in good agreement with the full shell model calculations reported in [17,41].

4.2. Results for Elastic Scattering

The DSM wave functions given by Equation (16) are used to calculate the normalized spin structure functions given in Equation (4) and also the squared nuclear form factors for these nuclei. Their values are plotted in Figure 5 as a function of u . The static spin matrix elements Ω_0 and Ω_1 for the ground state of ^{23}Na have values 0.727 and 0.652, respectively. They compare well with other theoretical calculations for ^{23}Na given in [17,41]. In order to compare our results with those of Klos [41], the calculated spin structure functions are transformed to structure factors $S_{\rho,\rho'}$ using the relation [34]

$$S_{\rho,\rho'} = \frac{1}{1 + \delta_{\rho,\rho'}} \frac{2J + 1}{8\pi} \Omega_\rho \Omega_{\rho'} F_{\rho,\rho'}. \quad (17)$$

Then, we evaluate $S_p = S_{00} + S_{01} + S_{11}$ and $S_n = S_{00} - S_{01} + S_{11}$ as defined by Klos et al. At $u = 0.5$, these values are 0.051 and 0.0002, which agree quite well with their result. Similarly at $u = 1$, the S_p and S_n have values of 0.027 and 0.0001. S_n is slightly smaller. At $u = 2$, $S_p = 0.021$ and $S_n = 0.0001$. Again at $u = 0.0$, $S_p = 0.15$ and $S_n = 0.001$ in agreement with the experiment. An analysis of the normalized spin structure functions for ^{23}Na in Figure 5 shows that the values of F_{00} , F_{01} and F_{11} differ between $u = 0.4$ – 3 . Outside this region they are almost degenerate. The form factors for proton and neutron in ^{23}Na are almost identical up to $u = 2$. Afterwards they differ and beyond $u = 2.6$, the neutron form factor becomes larger than the proton form factor.

The nuclear structure dependent coefficients given in Equation (8) are plotted in Figure 6 for ^{23}Na , as a function of the WIMP mass for different values of the detector threshold. Since Ω_0 and Ω_1 are of same sign, D_i s are all positive. The peaks of the nuclear structure coefficients occur at around $m_\chi \sim 30$ GeV at zero threshold energy. The peaks shift towards higher values of m_χ as we go to larger threshold energy. The thickness of the graphs represents annual modulation. Annual modulation has the largest value near the peaks of the graphs. Annual modulation provides strong evidence regarding the observation of dark matter since the background does not exhibit such modulation; see [13] for a recent review on annual modulation measurements. As seen from Figures 6 and 7, ^{23}Na shows that the percentage of annual modulation is almost the same as it is for heavier nuclei like ^{127}I , ^{133}Cs and ^{133}Xe reported in [12].

The event detection rates for these nuclei have been calculated at a particular WIMP mass by reading out the corresponding values of D_i 's from the Figure 6 and then evaluating Equation (7) for a given set of supersymmetric parameters. The event detection rates for different values of m_χ have been calculated using the nucleonic current parameters $f_A^0 = 3.55e - 2$, $f_A^1 = 5.31e - 2$, $f_S^0 = 8.02e - 4$ and $f_S^1 = -0.15 \times f_S^0$. These results are shown in Figure 7 for detector threshold energy $Q_{th} = 0, 10$ keV for ^{23}Na . For ^{23}Na , the peak occurs at $m_\chi \simeq 30$ GeV. The event rate decreases at higher detector threshold energy but the peak shifts to the higher values of m_χ occurring at ~ 50 GeV.

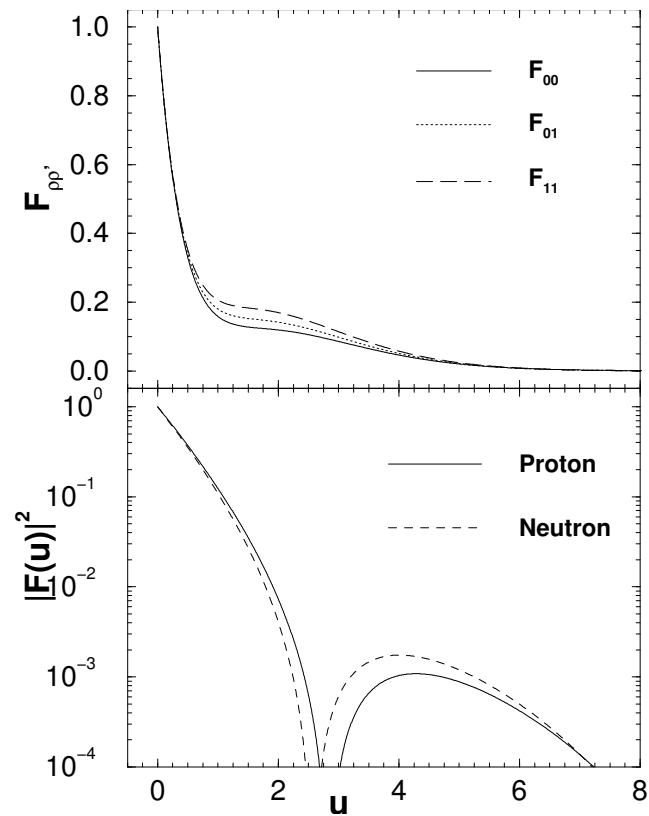


Figure 5. Spin structure functions and squared proton and neutron form factors for ^{23}Na for the ground state.

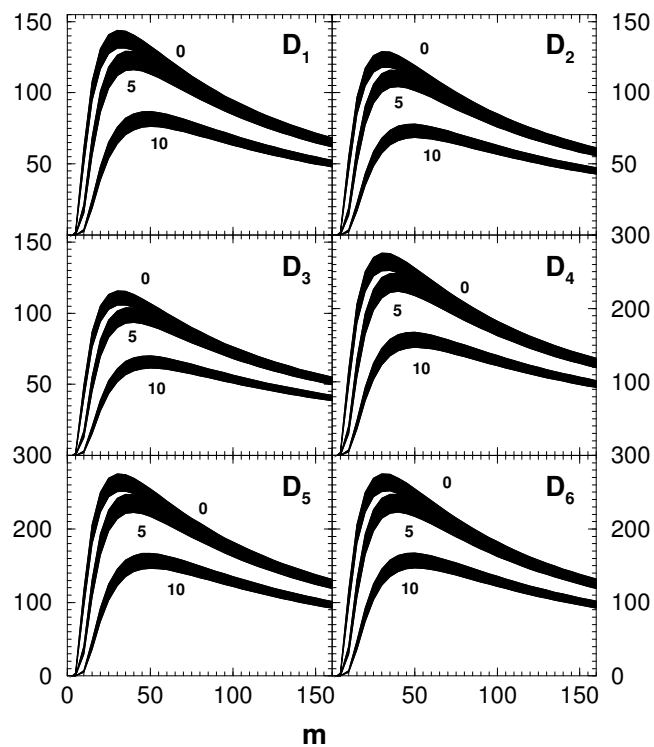


Figure 6. Nuclear structure coefficients plotted as a function of the Weakly Interacting Massive Particle (WIMP) mass in GeV for ^{23}Na . The graphs are plotted for three values of the detector threshold Q_{thr} namely $Q_{thr} = 0, 5, 10$ keV. The thickness of the graphs for each value of Q_{thr} represents the annual modulation.

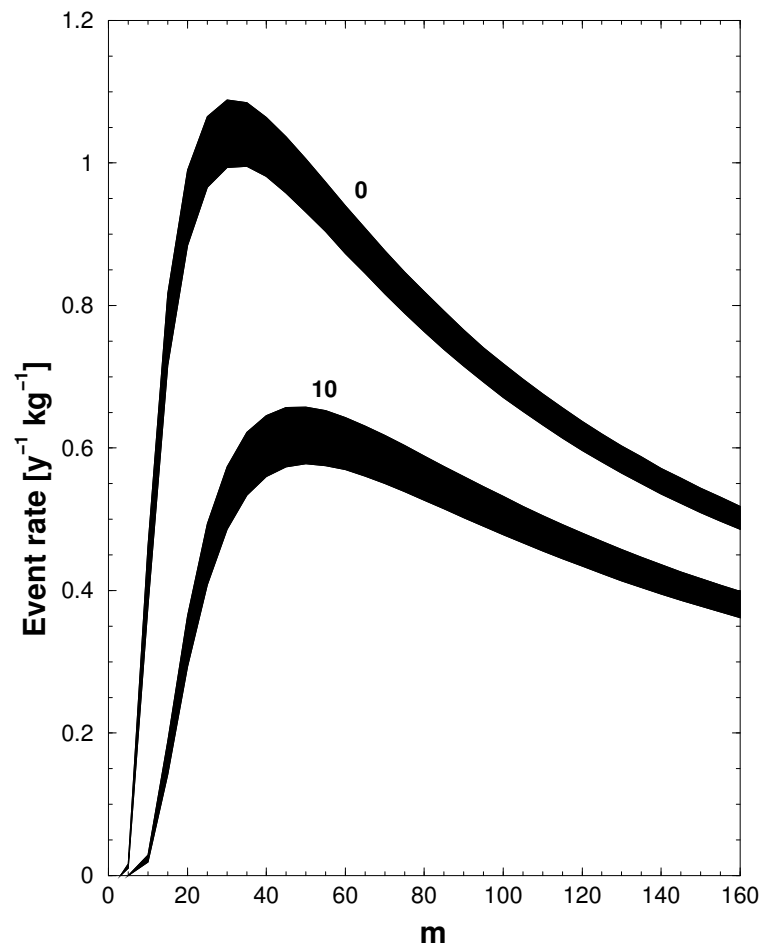


Figure 7. The event rates in units of $y^{-1} \text{ kg}^{-1}$ as a function of dark matter mass in GeV for ^{23}Na at detector threshold $Q_{th} = 0, 10$ keV. The thickness of the curves represents the annual modulation.

4.3. Results for Inelastic Scattering

^{23}Na has a $5/2^+$ excited state at 440 KeV above the ground state $3/2^+$. Therefore, we consider inelastic scattering from the ground state for this nucleus to the $5/2^+$ state. The static spin matrix elements for the inelastic scattering to the $J = 5/2^+$ are $\Omega_0 = -0.368$, $\Omega_1 = -0.462$. These values are of the same order of magnitude as for the elastic scattering case. Again Ω_0 and Ω_1 are of the same sign. The inelastic spin structure functions are given in Figure 8. In the figures, F_{00} , F_{01} and F_{11} are shown. The spin structure functions almost vanish above $u = 4$. With the value of u lying between 1 to 4, the spin structure functions differ from each other. The nuclear structure coefficients E_n are shown in Figure 9 for this nucleus. The inelastic nuclear structure coefficients do not depend on the detector threshold energy. Hence, the event rate can be calculated by reading the values of E_i from the graph and using the nucleonic current parameters. It is also seen that the percentage of annual modulation for the inelastic scattering case is not very much different than the elastic case (note that the scales in Figures 6 and 9 are different).

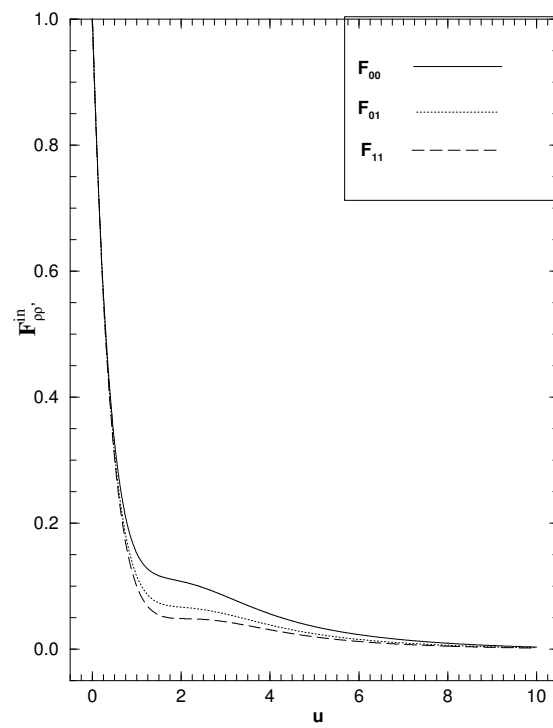


Figure 8. Spin structure function in the inelastic channel $3/2^+ \rightarrow 5/2^+$ for ^{23}Na .

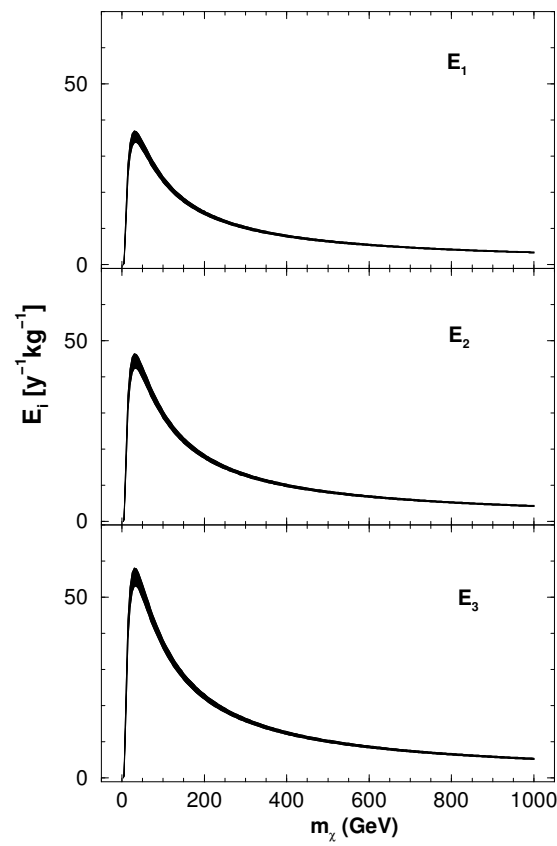


Figure 9. Nuclear structure coefficients E_n in the inelastic channel $3/2^+ \rightarrow 5/2^+$ for ^{23}Na . The thickness of the graphs represents annual modulation.

5. Results for WIMP-⁴⁰Ar Elastic Scattering

The event rates for WIMP-⁴⁰Ar elastic scattering are calculated using the nuclear wave functions generated through our DSM calculation. In our calculation, the active spherical single particles orbitals are taken as $0d_{5/2}$, $0d_{3/2}$, $1s_{1/2}$, $0f_{7/2}$, $0f_{5/2}$, $1p_{3/2}$ and $1p_{1/2}$ with ¹⁶O as the inert core. An effective interaction named $sdpf - u$ and developed by Nowacki and Poves [55] with single particle energies -3.699 , 1.895 , -2.915 , 6.220 , 11.450 , 6.314 and 6.479 MeV, respectively, for the above seven orbitals has been used. As discussed earlier, we first generate the lowest HF intrinsic state by solving the axially symmetric HF equation self-consistently. Then, we generate the excited configurations by particle-hole excitations. We have considered a total of nine intrinsic states. Good angular momentum states are projected from each of these intrinsic states and then a band mixing calculation is performed. The band mixed wave functions defined in Equation (16) are used in calculating the elastic event rates and nuclear structure coefficients for the ground state of this nucleus. Note that the ground state is a 0^+ state as ⁴⁰Ar is an even-even nucleus and inelastic scattering from ground needs an excited 1^+ state. However, the 1^+ states lie very high in energy and hence only elastic scattering of WIMP from ⁴⁰Ar is important. The oscillator length parameter b for this nucleus is taken to be 1.725 fm following the procedure mentioned in the beginning of Section 4. We have presented the proton and neutron form factors for the ground state of this nucleus in Figure 10. In addition, the nuclear structure dependent coefficients defined in Equation (8) are shown in Figure 11 for this nucleus as a function of the WIMP mass for different values of the detector threshold. Since ⁴⁰Ar is an even-even nucleus, there is no spin contribution from the ground state. Hence, we have only D_4 , D_5 and D_6 corresponding to the proton, neutron and proton-neutron form factors as defined in Equation (7). Their magnitudes are similar to the corresponding quantities in ²³Na and also the the percentage of annual modulation is almost same. The peaks occur at around $m_\chi = 35$ GeV. However, for larger values of Q_{thr} , the peaks shift towards the larger m_χ . It is important to add that the coefficients D_i in Figures 6 and 11 depend on the nuclear wave functions in addition to the WIMP velocity distribution. The nuclear structure part is in the u integration in Equations (5) and (8) but the limits of this integration depend on ψ and hence the nuclear structure part cannot be completely decoupled from the rest in the event rates calculations. The same is true for the structure factors E 's.

The event rates for WIMP-⁴⁰Ar scattering are plotted as a function of the dark matter mass in Figure 12 for $Q_{thr} = 0$ and 10 keV. The event rates are calculated using the same supersymmetric parameters as in ²³Na. The values are smaller than in ²³Na. This is because ⁴⁰Ar is an even-even nucleus and hence there is no spin contribution to the event rates in the ground state. At $Q_{thr} = 0$, the peak occurs at 35 GeV. For $Q_{thr} = 10$ keV, the peak shifts to 45 GeV.

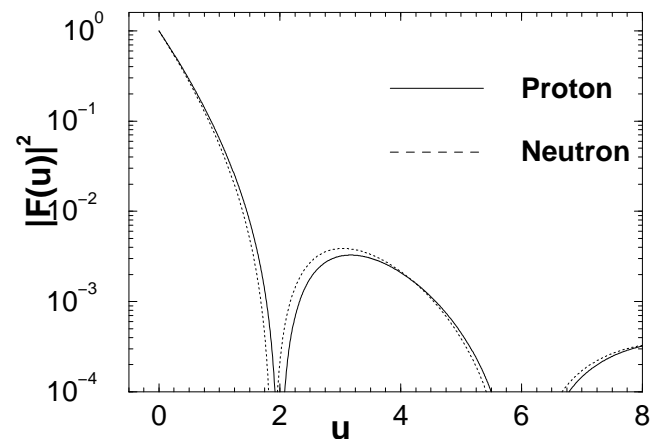


Figure 10. Squared proton and neutron form factors for ⁴⁰Ar for the ground state.

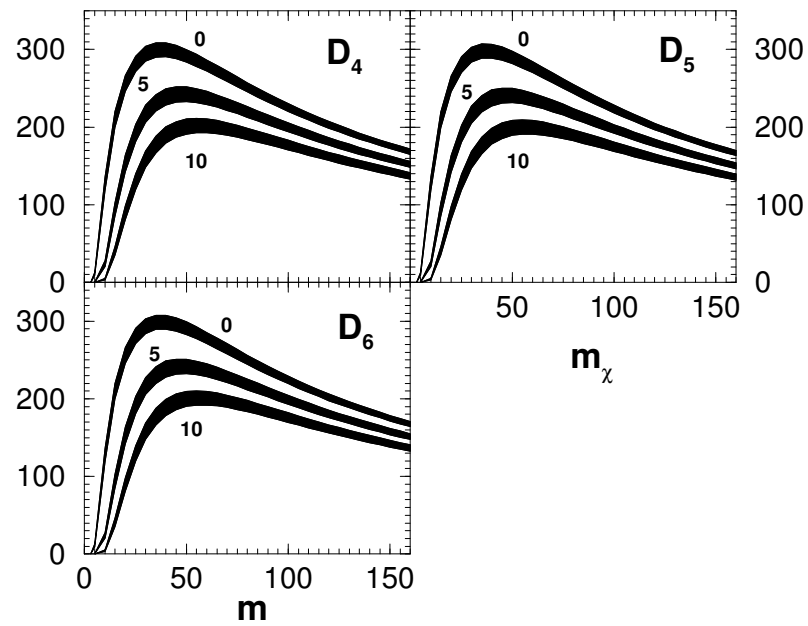


Figure 11. Nuclear structure coefficients plotted as a function of the WIMP mass m_χ in GeV for ^{40}Ar . The graphs are plotted for three values of the detector threshold Q_{thr} namely $Q_{thr} = 0, 5, 10$ keV. The thickness of the graphs for each value of Q_{thr} represents the annual modulation.

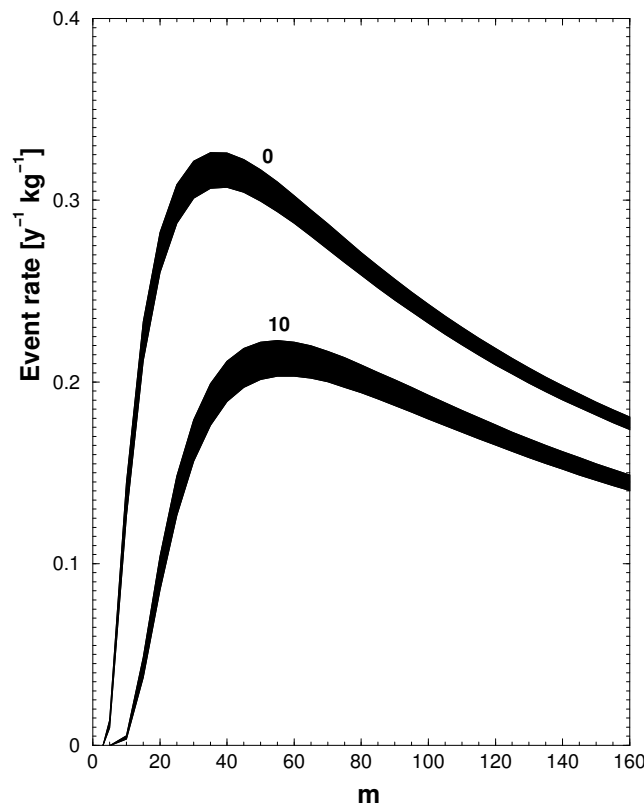


Figure 12. The event rates in units of $\text{y}^{-1} \text{kg}^{-1}$ as a function of dark matter mass m_χ in GeV for ^{40}Ar at detector threshold $Q_{th} = 0, 10$ keV. The thickness of the curves represent the annual modulation.

6. Summary and Conclusions

The deformed shell model is used to first calculate the event rates for the elastic and inelastic scattering of WIMP from ^{23}Na . At first, the reliability and effectiveness of DSM for spectroscopy is further tested by using ^{75}As as an example. Following this, spectroscopic properties ^{23}Na nucleus are calculated within DSM. We have also calculated magnetic

moments for the lowest level in this nucleus since spin plays an important role in the calculation of detection rates. After ensuring the good agreement with the experiment, we computed the spin structure functions, form factors, nuclear structure coefficients and the event rates for WIMP- ^{23}Na elastic and inelastic scattering. In addition, event rates for the elastic scattering of WIMP from ^{40}Ar are also presented. The results in Figures 7 and 12, for event rates, and in Figures 6, 7, 9, 11 and 12, for the annual modulation, we expect to be useful for the ongoing and future experiments looking for neutral current scattering events of CDM candidates with ^{23}Na and ^{40}Ar detector media.

Furthermore, using DSM for the nuclear structure aspects of the above promising CDM detectors, this study constitutes an extension of the investigation and the results presented for WIMP scattering off ^{73}Ge [49] and off ^{127}I , ^{133}Cs and ^{133}Xe [12]. Finally, we hope that our results combined with those obtained using other theoretical models for nuclear structure calculations may guide the experimentalists in their effort to unravel. In the near future, the fundamental mysteries of dark matter particles with the aid of tone scale detectors.

Author Contributions: All the authors contributed equally. All authors have read and agreed to the published version of the manuscript.

Funding: This research was funded by Department of Science and Technology (Government of India), and this research was co-financed by Greece and the European Union (European Social Fund-ESF) through the Operational Programme “Human Resources Development, Education and Lifelong Learning 2014–2020” in the context of the ESPA project MIS-5047635.

Data Availability Statement: All the numerical data for generating Figures 1–12 of the paper can be obtained from the first author R.S.

Acknowledgments: R.S. is thankful to SERB of Department of Science and Technology (Government of India) for financial support. T.S. Kosmas acknowledges that, this research is co-financed by Greece and the European Union (European Social Fund-ESF) through the Operational Programme “Human Resources Development, Education and Lifelong Learning 2014–2020” in the context of the ESPA project MIS-5047635.

Conflicts of Interest: The authors declare no conflict of interest.

References

- Smoot, G.F.; Bennett, C.L.; Kogut, A.; Wright, E.L.; Aymon, J.; Boggess, N.W.; Cheng, E.S.; De Amici, G.; Gulkis, S.; Hauser, M.G.; et al. Structure in the COBE Differential Microwave Radiometer First-Year Maps. *Astrophys. J. Lett.* **1992**, *396*, L1–L5. [[CrossRef](#)]
- Hinshaw, G.; Larson, D.; Komatsu, E.; Spergel, D.N.; Bennett, C.; Dunkley, J.; Nolte, M.R.; Halpern, M.; Hill, R.S.; Odegard, N.; et al. Nine-year Wilkinson Microwave Anisotropy Probe (WMAP) Observations: Cosmological Parameter Results (WMAP Collaboration). *Astrophys. J. Suppl.* **2013**, *208*, 19. [[CrossRef](#)]
- Aghanim, N.; Akrami, Y.; Ashdown, M.; Aumont, J.; Baccigalupi, C.; Ballardini, M.; Banday, A.J.; Barreiro, R.B.; Bartolo, N.; Basak, S. Planck 2018 results, VI. Cosmological parameters (Planck Collaboration). *Astronomy Astrophys.* **2020**, *641*, A6.
- Akrami, Y.; Ashdown, M.; Aumont, J.; Baccigalupi, C.; Ballardini, M.; Banday, A.J.; Barreiro, R.B.; Bartolo, N.; Basak, S.; Benabed, K.; et al. Planck 2018 results VII. Isotropy and statistics of the CMB (Planck Collaboration). *Astronomy Astrophys.* **2020**, *641*, A7.
- Jungman, G.; Kamionkowski, M.; Griest, K. Supersymmetric Dark Matter. *Phys. Rep.* **1996**, *267*, 195–373. [[CrossRef](#)]
- Gawiser, E.; Silk, J. Extracting primordial density fluctuations. *Science* **1998**, *280*, 1405–1411. [[CrossRef](#)] [[PubMed](#)]
- Du, N.; Force, N.; Khatriwada, R.; Lentz, E.; Ottens, R.; Rosenberg, L.J.; Rybka, G.; Carosi, G.; Woollett, N.; Bowring, D.; et al. Search for Invisible Axion Dark Matter with the Axion Dark Matter Experiment, (ADMX Collaboration). *Phys. Rev. Lett.* **2018**, *120*, 151301. [[CrossRef](#)]
- Kosmas, T.S.; Vergados, J.D. Cold dark matter in SUSY theories: The role of nuclear form factors and the folding with the LSP velocity. *Phys. Rev. D* **1997**, *55*, 1752–1764. [[CrossRef](#)]
- Vergados, J.D.; Kosmas, T.S. Searches for Cold Dark Matter: A Case of the Coexistence of Supersymmetry and Nuclear Physics. *Phys. Atom. Nucl.* **1998**, *61*, 1066–1080.
- Freese, K.; Lisanti, M.; Savage, C. Colloquium: Annual modulation of dark matter. *Rev. Mod. Phys.* **2013**, *85*, 1561–1581. [[CrossRef](#)]
- Liu, J.; Chen, X.; Ji, X. Current status of direct dark matter detection experiments. *Nat. Phys.* **2017**, *13*, 212–216. [[CrossRef](#)]
- Sahu, R.; Papoulias, D.K.; Kota, V.K.B.; Kosmas, T.S. Elastic and inelastic scattering of neutrinos and weakly interacting massive particles on nuclei. *Phys. Rev. C* **2020**, *102*, 035501. [[CrossRef](#)]
- Froberg, F.; Duffy, A.R. Annual modulation in direct dark matter searches. *J. Phys. G Nucl. Part. Phys.* **2020**, *47*, 094002. [[CrossRef](#)]

14. Aprile, E.; Aalbers, J.; Agostini, F.; Alfonsi, M.; Althueser, L.; Amaro, F.D.; Antochi, V.C.; Angelino, E.; Angevaere, J.R.; Arneodo, F.; et al. Observation of excess electronic recoil events in XENON1T (XENON Collaboration). *arXiv* **2020**, arXiv:2006.09721.
15. Amole, C.; Ardid, M.; Asner, D.M.; Baxter, D.; Behnke, E.; Bhattacharjee, P.; Borsodi, H.; Bou-Cabo, M.; Brice, S.J.; Broemmelsiek, D.; et al. Dark Matter Search Results from the PICO-60 C_3F_8 Bubble Chamber. *Phys. Rev. Lett.* **2017**, *118*, 251301. [[CrossRef](#)] [[PubMed](#)]
16. Broniatowski, A.; Defay, X.; Armengaud, E.; Berge, L.; Benoit, A.; Besida, O.; Blümer, J.; Chantelauze, A.; Chapellier, M.; Chardin, G.; et al. A new high-background-rejection dark matter Ge cryogenic detector (EDELWEISS Collaboration). *Phys. Lett. B* **2009**, *681*, 305–309. [[CrossRef](#)]
17. Divari, P.C.; Kosmas, T.S.; Vergados, J.D.; Skouras, I.D. Shell model calculations for light supersymmetric particle scattering off light nuclei. *Phys. Rev. C* **2000**, *61*, 054612. [[CrossRef](#)]
18. Bernabei, R.; Belli, P.; Bussolotti, A.; Cappella, F.; Caracciolo, V.; Cerulli, R.; Dai, C.J.; d'Angelo, A.; Di Marco, A.; He, H.L.; et al. First model independent results from DAMA/LIBRA-phase2. *Nucl. Phys. At. Energy* **2018**, *19*, 307–325. [[CrossRef](#)]
19. Bernabei, R.; Belli, P.; Cappella, F.; Cerulli, R.; Dai, C.J.; D'angelo, A.; He, H.L.; Incicchitti, A.; Kuang, H.H.; Ma, J.M.; et al. First results from DAMA/LIBRA and the combined results with DAMA/NaI. *Eur. Phys. J. C* **2008**, *56*, 333–355. [[CrossRef](#)]
20. Antonello, M.; Barberio, E.; Baroncelli, T.; Benziger, J.; Bignell, L.J.; Bolognino, I.; Calaprice, F.; Copello, S.; D'angelo, D.; DiImperio, G.; et al. The SABRE project and the SABRE Proof-of-Principle. *Eur. Phys. J. C* **2019**, *79*, 363. [[CrossRef](#)]
21. Amare, J.; Cebrian, S.; Cintas, D.; Coarasa, I.; Garcia, E.; Martinez, M.; Oliván, M.A.; Ortigoza, Y.; de Solorzano, A.O.; Puimedon, J.; et al. ANAIS-112 status: Two years results on annual modulation. *arXiv* **2019**, arXiv:1910.13365.
22. Adhikari, G.; Adhikari, P.; de Souza, E.B.; Carlin, N.; Choi, S.; Djamel, M.; Ezeribe, A.C.; Hyon Ha, C.; Hahn, I.; Hubbard, A.J.F.; et al. An experiment to search for dark-matter interactions using sodium iodide detectors. *Nature* **2018**, *564*, 83–86.
23. Agnes, P.; Albuquerque, I.F.M.; Alexander, T.; Alton, A.K.; Araujo, G.R.; Asner, D.M.; Ave, M.; Back, H.O.; Baldin, B.; Batignani, G.; et al. Low-Mass Dark Matter Search with the DarkSide-50 Experiment. *Phys. Rev. Lett.* **2018**, *121*, 081307. [[CrossRef](#)] [[PubMed](#)]
24. Ajaj, R.; Amaudruz, P.-A.; Araujo, G.R.; Baldwin, M.; Batygov, M.; Beltran, B.; Bina, C.E.; Bonatt, J.; Boulay, M.G.; Broerman, B.; et al. Search for dark matter with a 231-day exposure of liquid argon using DEAP-3600 at SNOLAB. *Phys. Rev. D* **2019**, *100*, 022004. [[CrossRef](#)]
25. Aalseth, C.E.; Acerbi, F.; Agnes, P.; Albuquerque, I.F.M.; Alexander, T.; Alici, A.; Alton, A.K.; Antonioli, P.; Arcelli, S.; Ardito, R.; et al. DarkSide-20k: A 20 Tonne Two-Phase LAr TPC for Direct Dark Matter Detection at LNGS. *Eur. Phys. J. Plus* **2018**, *133*, 131. [[CrossRef](#)]
26. Papoulias, D.K.; Sahu, R.; Kosmas, T.S.; Kota, V.K.B.; Nayak, B. Novel Neutrino-Floor and Dark Matter Searches with Deformed Shell Model Calculations. *Adv. High Energy Phys.* **2018**, *2018*, 6031362. [[CrossRef](#)]
27. Smponias, T.; Kosmas, O.T. High Energy Neutrino Emission from Astrophysical Jets in the Galaxy. *Adv. High Energy Phys.* **2015**, *2015*, 921757. [[CrossRef](#)]
28. Smponias, T.; Kosmas, O.T. Neutrino Emission from Magnetized Microquasar Jets. *Adv. High Energy Phys.* **2017**, *2017*, 4962741. [[CrossRef](#)]
29. Kosmas, O.T.; Smponias, T. Simulations of Gamma-Ray Emission from Magnetized Microquasar Jets. *Adv. High Energy Phys.* **2018**, *2018*, 9602960. [[CrossRef](#)]
30. Akimov, D.; Albert, J.B.; An, P.; Awe, C.; Barbeau, P.S.; Becker, B.; Belov, V.; Brown, A.; Bolozdynya, A.; Cabrera-Palmer, B.; et al. Observation of coherent elastic neutrino-nucleus scattering. *Science* **2017**, *357*, 1123–1128. [[CrossRef](#)]
31. Fitzpatrick, A.L.; Haxton, W.; Katz, E.; Lubbers, N.; Xu, Y.; Cosmol, J. The effective field theory of dark matter direct detection. *Astropart. Phys.* **2013**, *2*, 004. [[CrossRef](#)]
32. Anand, N.; Fitzpatrick, A.L.; Haxton, W.C. Weakly interacting massive particle-nucleus elastic scattering response. *Phys. Rev. C* **2014**, *89*, 065501. [[CrossRef](#)]
33. Hoferichter, M.; Klos, P.; Menendez, J.; Schwenk, A. Nuclear structure factors for general spin-independent WIMP-nucleus scattering. *Phys. Rev. D* **2019**, *99*, 055031. [[CrossRef](#)]
34. Holmlund, E.; Kortelainen, M.; Kosmas, T.S.; Suhonen, J.; Toivanen, J. Microscopic calculation of the LSP detection rates for the ^{71}Ga , ^{73}Ge and ^{127}I dark-matter detectors. *Phys. Lett. B* **2004**, *584*, 31–39. [[CrossRef](#)]
35. Kortelainen, M.; Kosmas, T.S.; Suhonen, J.; Toivanen, J. Event rates for CDM detectors from large-scale shell-model calculations. *Phys. Lett. B* **2006**, *632*, 226–232. [[CrossRef](#)]
36. Toivanen, P.; Kortelainen, M.; Suhonen, J.; Toivanen, J. Large-scale shell-model calculations of elastic and inelastic scattering rates of lightest supersymmetric particles (LSP) on ^{127}I , ^{129}Xe , ^{131}Xe , and ^{133}Cs nuclei. *Phys. Rev. C* **2009**, *79*, 044302. [[CrossRef](#)]
37. Vergados, J.D.; Avignone, F.T., III; Pirinen, P.; Srivastava, P.C.; Kortelainen, M.; Suhonen, J. Theoretical direct WIMP detection rates for transitions to nuclear excited states. *Phys. Rev. D* **2015**, *92*, 015015. [[CrossRef](#)]
38. Pirinen, P.; Srivastava, P.C.; Suhonen, J.; Kortelainen, M. Shell-model study on event rates of lightest supersymmetric particles scattering off ^{83}Kr and ^{125}Te . *Phys. Rev. D* **2016**, *93*, 095012. [[CrossRef](#)]
39. Vergados, J.D.; Moustakidis, C.C.; Cheung, Y.K.E.; Ejiri, H.; Kim, Y.; Lee, J.Y. Light WIMP Searches Involving Electron Scattering. *Adv. High Energy Phys.* **2018**, *2018*, 6257198. [[CrossRef](#)]
40. Bernabei, R.; Belli, P.; Cappella, F.; Cerulli, R.; Dai, C.J.; He, H.L.; Incicchitti, A.; Kuang, H.H.; Ma, J.M.; Ma, X.H.; et al. Investigation on light dark matter. *Mod. Phys. Lett.* **2008**, *A23*, 2125–2140. [[CrossRef](#)]

41. Klos, P.; Menendez, J.; Gazit, D.; Schwenk, A. Large-scale nuclear structure calculations for spin-dependent WIMP scattering with chiral effective field theory currents. *Phys. Rev. D* **2013**, *88*, 083516. [[CrossRef](#)]
42. Baudis, L.; Kessler, G.; Klos, P.; Lang, R.F.; Menendez, J.; Reichard, S.; Schwenk, A. Signatures of Dark Matter Scattering Inelastically Off Nuclei. *Phys. Rev. D* **2013**, *88*, 115014. [[CrossRef](#)]
43. Payne, C.G.; Bacca, S.; Hagen, G.; Jiang, W.; Papenbrock, T. Coherent elastic neutrino-nucleus scattering on ^{40}Ar from first principles. *Phys. Rev. C* **2019**, *100*, 061304. [[CrossRef](#)]
44. Kota, V.K.B.; Sahu, R. *Structure of Medium Mass Nuclei: Deformed Shell Model and Spin-Isospin Interacting Boson Model*; CRC Press, Taylor and Francis group: Boca Raton, FL, USA, 2016.
45. Srivastava, P.C.; Sahu, R.; Kota, V.K.B. Shell model and deformed shell model spectroscopy of ^{62}Ga . *Eur. Phys. J. A* **2015**, *51*, 1–9. [[CrossRef](#)]
46. Sahu, R.; Srivastava, P.C.; Kota, V.K.B. Deformed shell model results for neutrinoless positron double beta decay of nuclei in the $A = 60\text{--}90$ region. *J. Phys. G: Nucl. Part. Phys.* **2013**, *40*, 095107. [[CrossRef](#)]
47. Sahu, R.; Kota, V.K.B. Deformed shell model results for neutrinoless double beta decay of nuclei in $A = 60\text{--}90$ region. *Int. J. Mod. Phys. E* **2015**, *24*, 1550022. [[CrossRef](#)]
48. Kosmas, T.S.; Faessler, A.; Sahu, R.; Transition matrix elements for $\mu - e$ conversion in ^{72}Ge using the deformed Hartree-Fock method. *Phys. Rev. C* **2003**, *68*, 054315. [[CrossRef](#)]
49. Sahu, R.; Kota, V.K.B. Deformed shell model study of event rates for WIMP- ^{73}Ge scattering. *Mod. Phys. Lett.* **2017**, *32*, 175021. [[CrossRef](#)]
50. Evans, N.W.; O'Hare, C.A.J.; McCabe, C. SHM $^{++}$: A Refinement of the Standard Halo Model for Dark Matter Searches in Light of the Gaia Sausage. *arXiv* **2018**, arXiv:1810.11468 .
51. Ahalpara, D.P.; Bhatt, K.H.; Sahu, R. Collective bands in ^{81}Sr . *J. Phys. G Nucl. Part. Phys.* **1985**, *11*, 735–744. [[CrossRef](#)]
52. Available online: <http://www.nndc.bnl.gov/> (accessed on 11 January 2021).
53. Coraggio, L.; De Angelis, L.; Fukui, T.; Gargano, A.; Itaco, N. Calculation of Gamow-Teller and two-neutrino double- β decay properties for ^{130}Te and ^{136}Xe with a realistic nucleon-nucleon potential. *Phys. Rev. C* **2017**, *95*, 064324. [[CrossRef](#)]
54. Brown, B.A.; Wildenthal, B.H. Status of the nuclear shell model. *Annu. Rev. Nucl. Part. Sci.* **1988**, *38*, 29–66. [[CrossRef](#)]
55. Nowacki, F.; Poves, A. A new effective interaction for $0\hbar\omega$ shell-model calculations in the *sdpf* valence space. *Phys. Rev. C* **2009**, *79*, 014310. [[CrossRef](#)]